

Measurement of the ϕ_η^* distribution of muon pairs with masses between 30 and 500 GeV in 10.4 fb^{-1} of $p\bar{p}$ collisions

V. M. Abazov,³¹ B. Abbott,⁶⁷ B. S. Acharya,²⁵ M. Adams,⁴⁶ T. Adams,⁴⁴ J. P. Agnew,⁴¹ G. D. Alexeev,³¹ G. Alkhalaf,³⁵ A. Alton,^{56,a} A. Askew,⁴⁴ S. Atkins,⁵⁴ K. Augsten,⁷ C. Avila,⁵ F. Badaud,¹⁰ L. Bagby,⁴⁵ B. Baldin,⁴⁵ D. V. Bandurin,⁷³ S. Banerjee,²⁵ E. Barberis,⁵⁵ P. Baringer,⁵³ J. F. Bartlett,⁴⁵ U. Bassler,¹⁵ V. Bazterra,⁴⁶ A. Bean,⁵³ M. Begalli,² L. Bellantoni,⁴⁵ S. B. Beri,²³ G. Bernardi,¹⁴ R. Bernhard,¹⁹ I. Bertram,³⁹ M. Besançon,¹⁵ R. Beuselinck,⁴⁰ P. C. Bhat,⁴⁵ S. Bhatia,⁵⁸ V. Bhatnagar,²³ G. Blazey,⁴⁷ S. Blessing,⁴⁴ K. Bloom,⁵⁹ A. Boehnlein,⁴⁵ D. Boline,⁶⁴ E. E. Boos,³³ G. Borissov,³⁹ M. Borysova,^{38,l} A. Brandt,⁷⁰ O. Brandt,²⁰ R. Brock,⁵⁷ A. Bross,⁴⁵ D. Brown,¹⁴ X. B. Bu,⁴⁵ M. Buehler,⁴⁵ V. Buescher,²¹ V. Bunichev,³³ S. Burdin,^{39,b} C. P. Buszello,³⁷ E. Camacho-Pérez,²⁸ B. C. K. Casey,⁴⁵ H. Castilla-Valdez,²⁸ S. Caughron,⁵⁷ S. Chakrabarti,⁶⁴ K. M. Chan,⁵¹ A. Chandra,⁷² E. Chapon,¹⁵ G. Chen,⁵³ S. W. Cho,²⁷ S. Choi,²⁷ B. Choudhary,²⁴ S. Cihangir,⁴⁵ D. Claes,⁵⁹ J. Clutter,⁵³ M. Cooke,^{45,k} W. E. Cooper,⁴⁵ M. Corcoran,⁷² F. Couderc,¹⁵ M.-C. Cousinou,¹² D. Cutts,⁶⁹ A. Das,⁷¹ G. Davies,⁴⁰ S. J. de Jong,^{29,30} E. De La Cruz-Burelo,²⁸ F. Déliot,¹⁵ R. Demina,⁶³ D. Denisov,⁴⁵ S. P. Denisov,³⁴ S. Desai,⁴⁵ C. Deterre,^{41,c} K. DeVaughan,⁵⁹ H. T. Diehl,⁴⁵ M. Diesburg,⁴⁵ P. F. Ding,⁴¹ A. Dominguez,⁵⁹ A. Dubey,²⁴ L. V. Dudko,³³ A. Duperrin,¹² S. Dutt,²³ M. Eads,⁴⁷ D. Edmunds,⁵⁷ J. Ellison,⁴³ V. D. Elvira,⁴⁵ Y. Enari,¹⁴ H. Evans,⁴⁹ V. N. Evdokimov,³⁴ A. Fauré,¹⁵ L. Feng,⁴⁷ T. Ferbel,⁶³ F. Fiedler,²¹ F. Filthaut,^{29,30} W. Fisher,⁵⁷ H. E. Fisk,⁴⁵ M. Fortner,⁴⁷ H. Fox,³⁹ S. Fuess,⁴⁵ P. H. Garbincius,⁴⁵ A. Garcia-Bellido,⁶³ J. A. García-González,²⁸ V. Gavrilov,³² W. Geng,^{12,57} C. E. Gerber,⁴⁶ Y. Gershtein,⁶⁰ G. Ginther,^{45,63} O. Gogota,³⁸ G. Golovanov,³¹ P. D. Grannis,⁶⁴ S. Greder,¹⁶ H. Greenlee,⁴⁵ G. Grenier,¹⁷ Ph. Gris,¹⁰ J.-F. Grivaz,¹³ A. Grohsjean,^{15,c} S. Grünendahl,⁴⁵ M. W. Grünewald,²⁶ T. Guillemain,¹³ G. Gutierrez,⁴⁵ P. Gutierrez,⁶⁷ J. Haley,⁶⁸ L. Han,⁴ K. Harder,⁴¹ A. Harel,⁶³ J. M. Hauptman,⁵² J. Hays,⁴⁰ T. Head,⁴¹ T. Hebbeker,¹⁸ D. Hedin,⁴⁷ H. Hegab,⁶⁸ A. P. Heinson,⁴³ U. Heintz,⁶⁹ C. Hensel,¹ I. Heredia-De La Cruz,^{28,d} K. Herner,⁴⁵ G. Hesketh,^{41,f} M. D. Hildreth,⁵¹ R. Hirosky,⁷³ T. Hoang,⁴⁴ J. D. Hobbs,⁶⁴ B. Hoeneisen,⁹ J. Hogan,⁷² M. Hohlfeld,²¹ J. L. Holzbauer,⁵⁸ I. Howley,⁷⁰ Z. Hubacek,^{7,15} V. Hynek,⁷ I. Iashvili,⁶² Y. Ilchenko,⁷¹ R. Illingworth,⁴⁵ A. S. Ito,⁴⁵ S. Jabeen,^{45,m} M. Jaffré,¹³ A. Jayasinghe,⁶⁷ M. S. Jeong,²⁷ R. Jesik,⁴⁰ P. Jiang,⁴ K. Johns,⁴² E. Johnson,⁵⁷ M. Johnson,⁴⁵ A. Jonckheere,⁴⁵ P. Jonsson,⁴⁰ J. Joshi,⁴³ A. W. Jung,⁴⁵ A. Juste,³⁶ E. Kajfasz,¹² D. Karmanov,³³ I. Katsanos,⁵⁹ M. Kaur,²³ R. Kehoe,¹² S. Kermiche,¹² N. Khalatyan,⁴⁵ A. Khanov,⁶⁸ A. Kharchilava,⁶² Y. N. Kharzheev,³¹ I. Kiselevich,³² J. M. Kohli,²³ A. V. Kozelov,³⁴ J. Kraus,⁵⁸ A. Kumar,⁶² A. Kupco,⁸ T. Kurča,¹⁷ V. A. Kuzmin,³³ S. Lammers,⁴⁹ P. Lebrun,¹⁷ H. S. Lee,²⁷ S. W. Lee,⁵² W. M. Lee,⁴⁵ X. Lei,⁴² J. Lellouch,¹⁴ D. Li,¹⁴ H. Li,⁷³ L. Li,⁴³ Q. Z. Li,⁴¹ X. Li,⁴¹ J. K. Lim,²⁷ D. Lincoln,⁴⁵ J. Linnemann,⁵⁷ V. V. Lipaev,³⁴ R. Lipton,⁴⁵ H. Liu,⁷¹ Y. Liu,⁴ A. Lobodenko,³⁵ M. Lokajicek,⁸ R. Lopes de Sa,⁴⁵ R. Luna-Garcia,^{28,g} A. L. Lyon,⁴⁵ A. K. A. Maciel,¹ R. Madar,¹⁹ R. Magaña-Villalba,²⁸ S. Malik,⁵⁹ V. L. Malyshev,³¹ J. Mansour,²⁰ J. Martínez-Ortega,²⁸ R. McCarthy,⁶⁴ C. L. McGivern,⁴¹ M. M. Meijer,^{29,30} A. Melnitchouk,⁴⁵ D. Menezes,⁴⁷ P. G. Mercadante,³ M. Merkin,³³ A. Meyer,¹⁸ J. Meyer,^{20,1} F. Miconi,¹⁶ N. K. Mondal,²⁵ M. Mulhearn,⁷³ E. Nagy,¹² M. Narain,⁶⁹ R. Nayyar,⁴² H. A. Neal,⁵⁶ J. P. Negret,⁵ P. Neustroev,³⁵ H. T. Nguyen,⁷³ T. Nunnemann,²² J. Orduna,⁷² N. Osman,¹² J. Osta,⁵¹ A. Pal,⁷⁰ N. Parashar,⁵⁰ V. Parihar,⁶⁹ S. K. Park,²⁷ R. Partridge,^{69,e} N. Parua,⁴⁹ A. Patwa,^{65,j} B. Penning,⁴⁵ M. Perfilov,³³ Y. Peters,⁴¹ K. Petridis,⁴¹ G. Petrillo,⁶³ P. Pétrouff,¹³ M.-A. Pleier,⁶⁵ V. M. Podstavkov,⁴⁵ A. V. Popov,³⁴ M. Prewitt,⁷² D. Price,⁴¹ N. Prokopenko,³⁴ J. Qian,⁵⁶ Y. Qin,⁴¹ A. Quadt,²⁰ B. Quinn,⁵⁸ P. N. Ratoff,³⁹ I. Razumov,³⁴ I. Ripp-Baudot,¹⁶ F. Rizatdinova,⁶⁸ M. Rominsky,⁴⁵ A. Ross,³⁹ C. Royon,¹⁵ P. Rubinov,⁴⁵ R. Ruchti,⁵¹ G. Sajot,¹¹ A. Sánchez-Hernández,²⁸ M. P. Sanders,²² A. S. Santos,^{1,h} G. Savage,⁴⁵ M. Savitskiy,³⁸ L. Sawyer,⁵⁴ T. Scanlon,⁴⁰ R. D. Schamberger,⁶⁴ Y. Scheglov,³⁵ H. Schellman,⁴⁸ C. Schwanenberger,⁴¹ R. Schwienhorst,⁵⁷ J. Sekaric,⁵³ H. Severini,⁶⁷ E. Shabalina,²⁰ V. Shary,¹⁵ S. Shaw,⁴¹ A. A. Shchukin,³⁴ V. Simak,⁷ P. Skubic,⁶⁷ P. Slatery,⁶³ D. Smirnov,⁵¹ G. R. Snow,⁵⁹ J. Snow,⁶⁶ S. Snyder,⁶⁵ S. Söldner-Rembold,⁴¹ L. Sonnenschein,¹⁸ K. Soustruznik,⁶ J. Stark,¹¹ D. A. Stoyanova,³⁴ M. Strauss,⁶⁷ L. Suter,⁴¹ P. Svoisky,⁶⁷ M. Titov,¹⁵ V. V. Tokmenin,³¹ Y.-T. Tsai,⁶³ D. Tsybychev,⁶⁴ B. Tuchming,¹⁵ C. Tully,⁶¹ L. Uvarov,³⁵ S. Uvarov,³⁵ S. Uzunyan,⁴⁷ R. Van Kooten,⁴⁹ W. M. van Leeuwen,²⁹ N. Varelas,⁴⁶ E. W. Varnes,⁴² I. A. Vasilyev,³⁴ A. Y. Verkhnev,³¹ L. S. Vertogradov,³¹ M. Verzocchi,⁴⁵ M. Vesterinen,⁴¹ D. Vilanova,¹⁵ P. Vokac,⁷ H. D. Wahl,⁴⁴ M. H. L. S. Wang,⁴⁵ J. Warchol,⁵¹ G. Watts,⁷⁴ M. Wayne,⁵¹ J. Weichert,²¹ L. Welty-Rieger,⁴⁸ M. R. J. Williams,^{49,n} G. W. Wilson,⁵³ M. Wobisch,⁵⁴ D. R. Wood,⁵⁵ T. R. Wyatt,⁴¹ Y. Xie,⁴⁵ R. Yamada,⁴⁵ S. Yang,⁴ T. Yasuda,⁴⁵ Y. A. Yatsunenko,³¹ W. Ye,⁶⁴ Z. Ye,⁴⁵ H. Yin,⁴⁵ K. Yip,⁶⁵ S. W. Youn,⁴⁵ J. M. Yu,⁵⁶ J. Zennamo,⁶² T. G. Zhao,⁴¹ B. Zhou,⁵⁶ J. Zhu,⁵⁶ M. Zielinski,⁶³ D. Zieminska,⁴⁹ and L. Zivkovic¹⁴

(The D0 Collaboration)

¹LAFEX, Centro Brasileiro de Pesquisas Físicas, Rio de Janeiro, Brazil²Universidade do Estado do Rio de Janeiro, Rio de Janeiro, Brazil³Universidade Federal do ABC, Santo André, Brazil⁴University of Science and Technology of China, Hefei, People's Republic of China⁵Universidad de los Andes, Bogotá, Colombia

- ⁶*Faculty of Mathematics and Physics, Center for Particle Physics, Charles University, Prague, Czech Republic*
- ⁷*Czech Technical University in Prague, Prague, Czech Republic*
- ⁸*Institute of Physics, Academy of Sciences of the Czech Republic, Prague, Czech Republic*
- ⁹*Universidad San Francisco de Quito, Quito, Ecuador*
- ¹⁰*LPC, Université Blaise Pascal, CNRS/IN2P3, Clermont, France*
- ¹¹*LPSC, Université Joseph Fourier Grenoble 1, CNRS/IN2P3, Institut National Polytechnique de Grenoble, Grenoble, France*
- ¹²*CPPM, Aix-Marseille Université, CNRS/IN2P3, Marseille, France*
- ¹³*LAL, Université Paris-Sud, CNRS/IN2P3, Orsay, France*
- ¹⁴*LPNHE, Universités Paris VI and VII, CNRS/IN2P3, Paris, France*
- ¹⁵*CEA, Irfu, SPP, Saclay, France*
- ¹⁶*IPHC, Université de Strasbourg, CNRS/IN2P3, Strasbourg, France*
- ¹⁷*IPNL, Université Lyon 1, CNRS/IN2P3, Villeurbanne, France and Université de Lyon, Lyon, France*
- ¹⁸*III. Physikalisches Institut A, RWTH Aachen University, Aachen, Germany*
- ¹⁹*Physikalisches Institut, Universität Freiburg, Freiburg, Germany*
- ²⁰*II. Physikalisches Institut, Georg-August-Universität Göttingen, Göttingen, Germany*
- ²¹*Institut für Physik, Universität Mainz, Mainz, Germany*
- ²²*Ludwig-Maximilians-Universität München, München, Germany*
- ²³*Panjab University, Chandigarh, India*
- ²⁴*Delhi University, Delhi, India*
- ²⁵*Tata Institute of Fundamental Research, Mumbai, India*
- ²⁶*University College Dublin, Dublin, Ireland*
- ²⁷*Korea Detector Laboratory, Korea University, Seoul, Korea*
- ²⁸*CINVESTAV, Mexico City, Mexico*
- ²⁹*Nikhef, Science Park, Amsterdam, The Netherlands*
- ³⁰*Radboud University Nijmegen, Nijmegen, The Netherlands*
- ³¹*Joint Institute for Nuclear Research, Dubna, Russia*
- ³²*Institute for Theoretical and Experimental Physics, Moscow, Russia*
- ³³*Moscow State University, Moscow, Russia*
- ³⁴*Institute for High Energy Physics, Protvino, Russia*
- ³⁵*Petersburg Nuclear Physics Institute, St. Petersburg, Russia*
- ³⁶*Institució Catalana de Recerca i Estudis Avançats (ICREA) and Institut de Física d'Altes Energies (IFAE), Barcelona, Spain*
- ³⁷*Uppsala University, Uppsala, Sweden*
- ³⁸*Taras Shevchenko National University of Kyiv, Kiev, Ukraine*
- ³⁹*Lancaster University, Lancaster LA1 4YB, United Kingdom*
- ⁴⁰*Imperial College London, London SW7 2AZ, United Kingdom*
- ⁴¹*The University of Manchester, Manchester M13 9PL, United Kingdom*
- ⁴²*University of Arizona, Tucson, Arizona 85721, USA*
- ⁴³*University of California Riverside, Riverside, California 92521, USA*
- ⁴⁴*Florida State University, Tallahassee, Florida 32306, USA*
- ⁴⁵*Fermi National Accelerator Laboratory, Batavia, Illinois 60510, USA*
- ⁴⁶*University of Illinois at Chicago, Chicago, Illinois 60607, USA*
- ⁴⁷*Northern Illinois University, DeKalb, Illinois 60115, USA*
- ⁴⁸*Northwestern University, Evanston, Illinois 60208, USA*
- ⁴⁹*Indiana University, Bloomington, Indiana 47405, USA*
- ⁵⁰*Purdue University Calumet, Hammond, Indiana 46323, USA*
- ⁵¹*University of Notre Dame, Notre Dame, Indiana 46556, USA*
- ⁵²*Iowa State University, Ames, Iowa 50011, USA*
- ⁵³*University of Kansas, Lawrence, Kansas 66045, USA*
- ⁵⁴*Louisiana Tech University, Ruston, Louisiana 71272, USA*
- ⁵⁵*Northeastern University, Boston, Massachusetts 02115, USA*
- ⁵⁶*University of Michigan, Ann Arbor, Michigan 48109, USA*
- ⁵⁷*Michigan State University, East Lansing, Michigan 48824, USA*
- ⁵⁸*University of Mississippi, University, Mississippi 38677, USA*
- ⁵⁹*University of Nebraska, Lincoln, Nebraska 68588, USA*
- ⁶⁰*Rutgers University, Piscataway, New Jersey 08855, USA*
- ⁶¹*Princeton University, Princeton, New Jersey 08544, USA*
- ⁶²*State University of New York, Buffalo, New York 14260, USA*

⁶³University of Rochester, Rochester, New York 14627, USA⁶⁴State University of New York, Stony Brook, New York 11794, USA⁶⁵Brookhaven National Laboratory, Upton, New York 11973, USA⁶⁶Langston University, Langston, Oklahoma 73050, USA⁶⁷University of Oklahoma, Norman, Oklahoma 73019, USA⁶⁸Oklahoma State University, Stillwater, Oklahoma 74078, USA⁶⁹Brown University, Providence, Rhode Island 02912, USA⁷⁰University of Texas, Arlington, Texas 76019, USA⁷¹Southern Methodist University, Dallas, Texas 75275, USA⁷²Rice University, Houston, Texas 77005, USA⁷³University of Virginia, Charlottesville, Virginia 22904, USA⁷⁴University of Washington, Seattle, Washington 98195, USA

(Received 31 October 2014; revised manuscript received 17 February 2015; published 6 April 2015)

We present a measurement of the distribution of the variable ϕ_η^* for muon pairs with masses between 30 and 500 GeV, using the complete run II data set collected by the D0 detector at the Fermilab Tevatron proton-antiproton collider. This corresponds to an integrated luminosity of 10.4 fb^{-1} at $\sqrt{s} = 1.96 \text{ TeV}$. The data are corrected for detector effects and presented in bins of dimuon rapidity and mass. The variable ϕ_η^* probes the same physical effects as the Z/γ^* boson transverse momentum, but is less susceptible to the effects of experimental resolution and efficiency. These are the first measurements at any collider of the ϕ_η^* distributions for dilepton masses away from the $Z \rightarrow \ell^+\ell^-$ boson mass peak. The data are compared to QCD predictions based on the resummation of multiple soft gluons.

DOI: 10.1103/PhysRevD.91.072002

PACS numbers: 12.38.Qk, 13.85.Qk, 14.70.Hp

Drell-Yan lepton pairs are produced at hadron colliders via quark-antiquark annihilation and may be produced with a nonzero momentum in the plane transverse to the beam direction $p_T^{\ell\ell}$ ($\ell = e, \mu, \tau$) due to QCD radiation from the incoming partons. Measurements of $p_T^{\ell\ell}$ and related variables in events containing Drell-Yan lepton pairs thus allow models of initial-state QCD radiation to be tested. Such models are an important component in the

phenomenological interpretation of almost all experimental measurements and in searches for new physics at hadron colliders.

In Ref. [1] the D0 Collaboration used the variable ϕ_η^* [2] to study, with unprecedented precision, the $p_T^{\ell\ell}$ distribution of Z/γ^* bosons in dielectron and dimuon final states with dilepton invariant mass $M_{\ell\ell}$ close to the Z boson pole. The measurements were presented in bins of dilepton rapidity $|y|$ [3]. The variable ϕ_η^* is defined [2] as

$$\phi_\eta^* \equiv \tan(\phi_{\text{acop}}/2) \sin \theta_\eta^*, \quad (1)$$

where ϕ_{acop} is the acoplanarity angle, given by

$$\phi_{\text{acop}} = \pi - \Delta\phi^{\ell\ell}, \quad (2)$$

and $\Delta\phi^{\ell\ell}$ is the difference in azimuthal angle ϕ between the two lepton candidates. Figure 1 illustrates relevant variables in the plane transverse to the beam direction [1]. The variable θ_η^* is a measure of the scattering angle of the leptons with respect to the proton beam direction in the rest frame of the dilepton system. It is defined [2] by

$$\cos(\theta_\eta^*) = \tanh[(\eta^- - \eta^+)/2], \quad (3)$$

where η^- and η^+ are the pseudorapidities [4] of the negatively and positively charged lepton, respectively. The acoplanarity ϕ_{acop} gives the degree to which the two leptons deviate from being back to back in the plane transverse to the beam direction; it is thus related to $p_T^{\ell\ell}$. Multiplying by $\sin \theta_\eta^*$ in Eq. (1) corrects for the fact that

^aVisitor from Augustana College, Sioux Falls, SD, USA.^bVisitor from The University of Liverpool, Liverpool, United Kingdom.^cVisitor from DESY, Hamburg, Germany.^dVisitor from Universidad Michoacana de San Nicolas de Hidalgo, Morelia, Mexico.^eVisitor from SLAC, Menlo Park, CA, USA.^fVisitor from University College London, London, United Kingdom.^gVisitor from Centro de Investigacion en Computacion—IPN, Mexico City, Mexico.^hVisitor from Universidade Estadual Paulista, São Paulo, Brazil.ⁱVisitor from Karlsruhe Institut für Technologie (KIT)—Steinbuch Centre for Computing (SCC), D-76128 Karlsruhe, Germany.^jVisitor from Office of Science, U.S. Department of Energy, Washington, D.C. 20585, USA.^kVisitor from American Association for the Advancement of Science, Washington, D.C. 20005, USA.^lVisitor from Kiev Institute for Nuclear Research, Kiev, Ukraine.^mVisitor from University of Maryland, College Park, MD 20742, USA.ⁿVisitor from European Organization for Nuclear Research (CERN), Geneva, Switzerland.

even for fixed values of $M_{\ell\ell}$ and $p_T^{\ell\ell}$, events with different values of $\sin\theta_\eta^*$ will correspond to different values of ϕ_{acop} . The variable ϕ_η^* is therefore more closely related to $p_T^{\ell\ell}$ than is ϕ_{acop} . Since ϕ_{acop} and θ_η^* depend exclusively on the directions of the two leptons, which are typically determined with a precision of a milliradian or better, ϕ_η^* is experimentally very well measured compared to any quantities, such as $p_T^{\ell\ell}$, that rely on the momenta of the leptons.

The new experimental variables proposed in Ref. [2] and exploited by D0 in Ref. [1] have prompted a considerable amount of theoretical and experimental activity. For example, QCD calculations including the resummation of multiple soft gluon emissions at next-to-next-to-leading log (NNLL) accuracy [7,8] and matched to the next-to-leading order (NLO) Monte Carlo (MC) calculation MCFM [9] have been shown to be consistent with the D0 data [1] to within the assigned theoretical uncertainties. The D0 data [1] have been used as input to improve the predictions from the RESBOS MC program [10]. Predictions at NNLL + NLO accuracy for the distribution of ϕ_η^* of Z/γ^* bosons in proton-proton collisions at the LHC [11] have been made. Subsequent experimental measurements of the distribution of ϕ_η^* by the ATLAS Collaboration [12] in bins of dilepton rapidity are in agreement with these predictions. Complementary measurements of the distribution of ϕ_η^* for Z/γ^* bosons that are highly boosted along the LHC beam direction have been made by the LHCb Collaboration [13]. These measurements are also in reasonable agreement with predictions.

In this paper we present measurements of the normalized ϕ_η^* distribution of Drell-Yan muon pairs, $(1/\sigma) \times (d\sigma/d\phi_\eta^*)$, in bins of dimuon rapidity in $p\bar{p}$ collisions at $\sqrt{s} = 1.96$ TeV. We update the dimuon measurements of Ref. [1] for $70 < M_{\ell\ell} < 110$ GeV to the complete 10.4 fb^{-1} data set collected by the D0 detector during run 2 at the Fermilab Tevatron. In addition, we extend the measurements to “off-peak” samples of dimuon events and consider ranges of $M_{\ell\ell}$ between 30 and 500 GeV. These are the first measurements at any collider of the ϕ_η^* distributions of dileptons away from the Z boson mass peak.

As discussed in Ref. [2], ϕ_η^* is highly correlated with the quantity $a_T/M_{\ell\ell}$, where the variable a_T [5] corresponds to one of two orthogonal components of $p_T^{\ell\ell}$ (as illustrated in Fig. 1). The width of the $p_T^{\ell\ell}$ distribution is expected to increase approximately logarithmically with increasing $M_{\ell\ell}$. This is because the larger initial-state parton momenta required to produce heavier dilepton final states allow for harder initial-state radiation [14]. Therefore, the width of the ϕ_η^* distribution is expected to decrease with increasing $M_{\ell\ell}$. Measurements of the distribution of ϕ_η^* over a wide range of $M_{\ell\ell}$ values allow this prediction to be tested.

Initial-state gluon bremsstrahlung represents an important source of systematic uncertainty in analyses of high

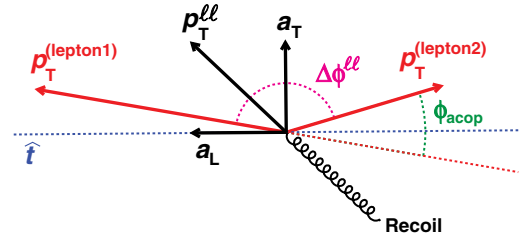


FIG. 1 (color online). Illustration in the plane transverse to the beam direction of the variables defined in the text and used to analyze the dilepton transverse momentum [1]. The variables a_T and a_L [5] correspond to the decomposition of $p_T^{\ell\ell}$ into two orthogonal components relative to the dilepton thrust axis \hat{t} [6], as illustrated.

mass final states at hadron colliders, such as those containing top quarks. It is therefore interesting to use the ϕ_η^* distribution of high mass dilepton final states to test QCD descriptions of initial-state gluon bremsstrahlung in the relevant mass range.

D0 [15] is a general purpose detector located at the Fermilab Tevatron proton-antiproton collider. The detector has a central-tracking system, consisting of a silicon microstrip tracker and a central fiber tracker, both located within a 1.9 T superconducting solenoidal magnet, with designs optimized for tracking for $|\eta| < 3$. A liquid-argon and uranium calorimeter has a central section covering $|\eta| < 1.1$, and two end calorimeters that extend coverage to $|\eta| \approx 4.2$, with all three housed in separate cryostats [16]. An outer muon system, at $|\eta| < 2$, consists of a layer of tracking detectors and scintillation trigger counters in front of 1.8 T iron toroidal magnets, followed by two similar layers after the toroids [17].

Drell-Yan dimuon MC events are generated with PYTHIA [18] and passed through a GEANT-based [19] simulation of the detector. Backgrounds from $Z/\gamma^* \rightarrow \tau^-\tau^+$, $W \rightarrow \ell\nu$ (+jets), and $WW \rightarrow \ell\nu\ell\nu$ are simulated using PYTHIA. Background from top quark pair production is simulated with ALPGEN [20], with PYTHIA used for parton showering. To simulate the effects of additional proton-antiproton interactions and detector noise, events from randomly triggered beam crossings collected during normal data taking are added to the simulated events. Background from multijet events is estimated from the data using samples of events containing poorly isolated muons and same-sign muon pairs.

A second sample of Drell-Yan dimuon MC events (without detector simulation) is generated using RESBOS [21]. RESBOS generates Z boson production with initial-state QCD corrections approximately to next-to-next-to-leading order (NNLO) by using approximate NNLO Wilson coefficient functions [10], and full NNLL accuracy to account for contributions of soft gluon emission [10,21]. The γ^* and Z/γ^* interference contributions are included with initial-state QCD corrections to NLO and NNLL accuracy. The RESBOS prediction uses the

Guzzi-Nadolsky-Wang [10,21] nonperturbative function for the region of small $p_T^{\ell\ell}$, which is controlled by the parameter a_Z . In our choice of central values and systematic variations [22] for QCD scales and a_Z we follow Ref. [10]. The CT10 NNLO parton distribution functions (PDFs) [23] are used and the effects of final-state photon radiation (FSR) are taken from PHOTOS [24].

In addition to RESBOS, we compare our corrected data to the NNLL + NLO predictions of Ref. [8]. The NLO PDF sets CTEQ6 m [25] are implemented in this calculation. The NNLL + NLO predictions of Ref. [8] do not include the effects of FSR. The QCD scales are set event by event to the mass of the Z/γ^* boson propagator.

Candidate dimuon events are required to satisfy a trigger based on the identification of a single muon and to contain two reconstructed muons. One of the muons is required to have reconstructed track segments in the muon system tracking detectors both inside and outside the toroidal magnets. The second muon is required to have hits in the muon system or to have an energy deposit in the calorimeter that is consistent with the passage of a minimum-ionizing particle. To ensure an accurate measurement of the muon directions, the two muon candidates are required to be matched to a pair of particle tracks reconstructed in the central tracking detectors with momentum transverse to the beam direction of $p_T > 15$ GeV and $|\eta| < 2$. Candidate muons resulting from misidentified hadrons or produced by the decay of hadrons are suppressed by requiring that they be isolated from other particles observed in either the central-tracking detectors or the calorimeters. Requirements are placed on the sum of the p_T of tracks within a cone of $\Delta R = \sqrt{(\Delta\eta)^2 + (\Delta\phi)^2} < 0.5$ around the muon track and on the sum of the E_T of calorimeter clusters within an annulus $0.1 < \Delta R < 0.4$ around the muon track. If more than two muon candidates satisfying the above criteria are found, the two with the highest p_T are considered. The muon tracks are required to be oppositely charged.

Contamination from cosmic ray muons is eliminated by requiring that the muons originate from the $p\bar{p}$ collision point on the basis of their impact parameters and times of flight, and by rejecting events in which the two muon candidates are back to back in η within the experimental resolution.

For $70 < M_{\ell\ell} < 110$ GeV a total of 645 k dimuon events is selected and the total background fraction, arising mainly from multijet events, is 0.2%.

Away from the Z boson mass peak it is more difficult to obtain samples of well-measured Drell-Yan dimuon events with acceptable levels of background, and additional event selection criteria are imposed. An important source of contamination in the off-peak samples arises from Drell-Yan dimuon events that at Born level have a Z/γ^* boson mass outside the selected range in $M_{\ell\ell}$, but are reconstructed with a value of $M_{\ell\ell}$ within the selected range due

to FSR or to the mismeasurement of the p_T of one of the muon candidates. We refer below to such events as arising from ‘‘bin migration in $M_{\ell\ell}$.’’ The levels of bin migration in the off-peak signal samples are estimated and corrected for using the Drell-Yan dimuon MC and are cross-checked using control samples in the data.

Below the Z boson mass peak, dimuon events are selected with $30 < M_{\ell\ell} < 60$ GeV. To increase the event selection efficiency in this low mass region and to reduce any kinematic bias on the distribution of ϕ_{η}^* , the selection criteria are relaxed: we require the leading muon to satisfy $p_T > 15$ GeV, but allow the second muon to satisfy $p_T > 10$ GeV. The dominant backgrounds in the $30 < M_{\ell\ell} < 60$ GeV sample arise from $Z/\gamma^* \rightarrow \tau^-\tau^+$ and bin migration in $M_{\ell\ell}$. Background from $Z/\gamma^* \rightarrow \tau^-\tau^+$ events containing hadronically decaying τ leptons is suppressed by applying isolation criteria on the muon candidates that are more stringent than those used for the $70 < M_{\ell\ell} < 110$ GeV event sample. In particular, an additional requirement is placed on the sum of the E_T of calorimeter clusters within a cone $\Delta R < 0.1$ around the muon track. The fraction of the selected event sample arising from $Z/\gamma^* \rightarrow \tau^-\tau^+$ background is estimated to be 5.2%. The number of selected events that originate close to the Z boson mass peak but are reconstructed with $30 < M_{\ell\ell} < 60$ GeV due to FSR is reduced by excluding events that contain an isolated photon candidate with $p_T > 15$ GeV. Bin migration in $M_{\ell\ell}$ from the Z boson mass peak can also arise from events in which the p_T of one of the muon candidates is underestimated. This is suppressed using a ‘‘pseudomass’’ variable, M_{pseudo} : the invariant mass of the muon pair is recalculated having set the magnitude of the p_T of the lower p_T muon to be equal to that of the higher p_T muon. This is under the hypothesis that if an event originates close to the Z boson mass peak, but is reconstructed with $30 < M_{\ell\ell} < 60$ GeV, the p_T of the lower p_T muon candidate has been underestimated. Events arising from bin migration in $M_{\ell\ell}$ tend to have large values of M_{pseudo} and candidate events are required to satisfy $M_{\text{pseudo}} < 75$ GeV. This requirement rejects only 2% of Drell-Yan dimuon events with $30 < M_{\ell\ell} < 60$ GeV at the generator level. The fraction of the selected event sample arising from Drell-Yan dimuon events for which the Born level Z/γ^* boson propagator mass is greater than 70 GeV is estimated to be 1.3%. Remaining backgrounds amount to 1.6% of the selected event sample and arise mainly from multijet events. A total of 74 k dimuon events is selected for $30 < M_{\ell\ell} < 60$ GeV.

Above the Z boson mass peak, dimuon events are selected within the two mass ranges $160 < M_{\ell\ell} < 300$ GeV and $300 < M_{\ell\ell} < 500$ GeV. In these samples the only significant source of contamination arises from the moderate resolution in p_T (and thus $M_{\ell\ell}$) in the compact central-tracking detectors of $D\phi$. The level of bin migration in $M_{\ell\ell}$ in Drell-Yan dimuon events is reduced by imposing

tight requirements on the number of silicon microstrip and central fiber tracker hits associated with the muon tracks and the χ^2 of the track fits. Bin migration in $M_{\ell\ell}$ is further suppressed by rejecting events in which there is a very large asymmetry between the magnitudes of the p_T of the two muons. Specifically, it is required that

$$\frac{|\Delta p_T|}{m_{\ell\ell}^2} < 0.004e^{-M_{\ell\ell}/80} + 0.00115,$$

where Δp_T is the difference in the magnitudes of the p_T of the two muons, and the units of Δp_T and $M_{\ell\ell}$ are GeV. For the mass ranges $160 < M_{\ell\ell} < 300$ GeV and $300 < M_{\ell\ell} < 500$ GeV, respectively, the numbers of selected events are 1744 and 207, and the fractions of the selected event samples arising from bin migration in $M_{\ell\ell}$ are estimated to be 24 and 44%.

The observed ϕ_η^* distributions are corrected for background, and for experimental efficiency and resolution. Backgrounds from $Z/\gamma^* \rightarrow \tau^-\tau^+$, $W \rightarrow \ell\nu$ (+jets), $WW \rightarrow \ell\nu\ell\nu$, top quark pairs and multijet events are subtracted from the observed ϕ_η^* distributions. The corrections to the background-subtracted ϕ_η^* distribution for experimental efficiency and resolution (including the effect of bin migration in $M_{\ell\ell}$) are evaluated using fully simulated dimuon MC events. When evaluating the correction factors, we apply at the MC particle level the same kinematic selection criteria on $M_{\ell\ell}$, muon p_T , and $|\eta|$ as in the selection of the data, as specified above. For this purpose, MC particle-level muons are defined after QED final-state radiation, which mimics the measurement of muon momentum in the tracking detector. In addition, in the low mass dimuon sample ($30 < M_{\ell\ell} < 60$ GeV) events are rejected if they contain an FSR photon with transverse energy $E_T^\gamma > 14$ GeV; this is in order to mimic the selection criteria on isolated photons and muon isolation applied at the detector level.

Since the experimental resolution in ϕ_η^* is narrower than the chosen bin widths, the fractions of accepted events that fall within the same bin in ϕ_η^* at the particle level and reconstructed detector level in the MC are high, having typical (lowest) values of around 98% (92%). Therefore, simple bin-by-bin corrections of the ϕ_η^* distribution are sufficient.

The fully simulated Drell-Yan dimuon MC events used to calculate the detector corrections are reweighted at the generator level in two dimensions ($p_T^{\ell\ell}$ and $|y|$) to match the predictions of RESBOS. In addition, adjustments are made to improve the accuracy of the following aspects of the detector simulation: muon p_T scale and resolution, track ϕ and η resolutions, trigger efficiencies, and relevant offline reconstruction and selection efficiencies. Variations in the above adjustments to the underlying physics and the detector simulation are included in the assessment of the systematic uncertainties on the correction factors. Because

of the high bin purities, the systematic uncertainties on the correction factors arising from variations in the assumed underlying ϕ_η^* distribution are found to be negligible.

The systematic uncertainties due to muon p_T scale and resolution are small, and arise only due to the kinematic requirements in the event selection. The measured ϕ_η^* distribution is, however, susceptible to modulations in ϕ of the muon identification and trigger efficiencies, which result, e.g., from detector module boundaries in the muon system. Particular care has been taken in the choice of muon identification criteria in order to minimize such modulations and also to ensure that such modulations are well simulated in the MC. For example, the inclusion of muon candidates identified in the calorimeter reduces the effect of gaps between modules in the outer muon system. Nevertheless, accurate modeling of the residual inefficiencies in the intermodule regions is verified, since this is particularly important in this measurement; regions of low efficiency that are back to back in ϕ cause the efficiency to modulate as a function of ϕ_η^* . Accurate modeling of the angular resolution of the central-tracking detectors is another crucial aspect of this analysis. The resolution in ϕ and η is measured in the data using cosmic ray muons that traverse the detector, since these should produce events containing two tracks that are exactly back to back except for the effect of detector resolution.

Control samples in which one or more of the event selection criteria are relaxed or inverted are used to test the predicted levels of background in the off-peak dimuon samples and to assess the associated systematic uncertainties. The level of background in the $30 < M_{\ell\ell} < 60$ GeV sample arising from $Z/\gamma^* \rightarrow \tau^-\tau^+$ events containing hadronically decaying τ leptons is verified by checking that the simulation provides a good description of the sum of the E_T of calorimeter clusters within $\Delta R < 0.1$ around the muon track. In addition, hadrons misidentified as muons are less likely than genuine muons to be associated with reconstructed track segments in the muon system both inside and outside the toroidal magnets. The number and kinematic properties of events containing only one such muon candidate, which are enriched in $Z/\gamma^* \rightarrow \tau^-\tau^+$ events containing hadronically decaying τ leptons, are found to be reasonably well described.

In the off-peak samples the predicted levels of bin migration in $M_{\ell\ell}$ are cross-checked using control samples. For $30 < M_{\ell\ell} < 60$ GeV the number and kinematic properties of the events exclusively rejected by the veto on isolated photons are well described. The selection criteria on M_{pseudo} (for $30 < M_{\ell\ell} < 60$ GeV) and the asymmetry between the magnitudes of the p_T of the two muons (for $160 < M_{\ell\ell} < 300$ GeV and $300 < M_{\ell\ell} < 500$ GeV) introduce a bias on the ϕ_η^* distributions of the selected event samples, which has to be accounted for in the MC-derived correction factors. It has been verified that the distributions in M_{pseudo} and the p_T asymmetry, having

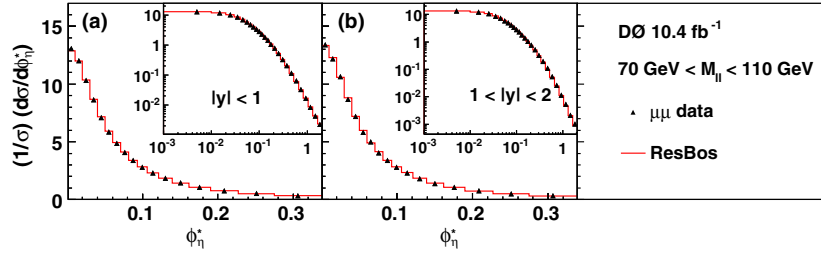


FIG. 2 (color online). Corrected distributions of $(1/\sigma) \times (d\sigma/d\phi_\eta^*)$ in dimuon events with $70 < M_{\ell\ell} < 110$ GeV for (a) $|y| < 1$ and (b) $1 < |y| < 2$ in the restricted range $0 < \phi_\eta^* < 0.34$. The insets show an extended range of ϕ_η^* . The error bars on the data points represent statistical and systematic uncertainties combined in quadrature. The predictions from RESBOS [10] are shown as histograms.

applied all other selection cuts, are reasonably well described by the MC.

Systematic uncertainties on the corrections applied to the data arise from residual uncertainties in the modeling of the detector response and the levels of backgrounds. The following are varied within their uncertainties: muon p_T scale and resolution; dependence of trigger and offline identification efficiencies on η and on the proximity to detector module boundaries in ϕ . Systematic uncertainties on the levels of backgrounds are assigned to cover the statistical uncertainties of the cross-checks using control samples, as well as any residual data-MC discrepancies revealed by these cross-checks. The total experimental systematic uncertainty is evaluated as the quadrature sum of all the uncertainties discussed above. In almost all ϕ_η^* bins the total experimental systematic uncertainty is substantially smaller than the statistical uncertainty.

The overall QCD uncertainty on the RESBOS predictions is taken as the quadrature sum of the changes in the predicted $(1/\sigma) \times (d\sigma/d\phi_\eta^*)$ resulting from variations in QCD scales, the nonperturbative parameter a_Z and PDFs. In our choice of systematic variations [22] for QCD scales and a_Z we follow Ref. [10]. Uncertainties due to PDFs are

evaluated using the CT10 NNLO error PDF sets [23]. In the predictions from RESBOS the uncertainties arising from QCD scales are typically a factor of around two larger than those arising from PDFs or a_Z . For the NNLL + NLO predictions, the theoretical uncertainties are assessed by variations in renormalization scale, factorization scale and resummation scale between $M_{\ell\ell}/2$ and $2M_{\ell\ell}$, with the additional requirement that the ratio of any two of these scales lies between $1/2$ and 2 [8].

Figure 2 shows the normalized dimuon ϕ_η^* distributions $(1/\sigma) \times (d\sigma/d\phi_\eta^*)$ in two bins of dimuon $|y|$ corrected to the particle level for the kinematic region: $70 < M_{\ell\ell} < 110$ GeV, and for both muons $p_T > 15$ GeV and $|\eta| < 2$. The data are compared to predictions from RESBOS for the same particle-level kinematic region and in the same bins used for the experimental data. The values of $(1/\sigma) \times (d\sigma/d\phi_\eta^*)$ are plotted at the center of the relevant bin in ϕ_η^* .

Figure 3 shows the ratio of the corrected ϕ_η^* distributions to the RESBOS predictions for $70 < M_{\ell\ell} < 110$ GeV. In addition to the dimuon data from the present analysis, the dielectron data from Ref. [1] are shown [26]. Given that the experimental corrections are very different in the two channels, the consistency of the dielectron and dimuon

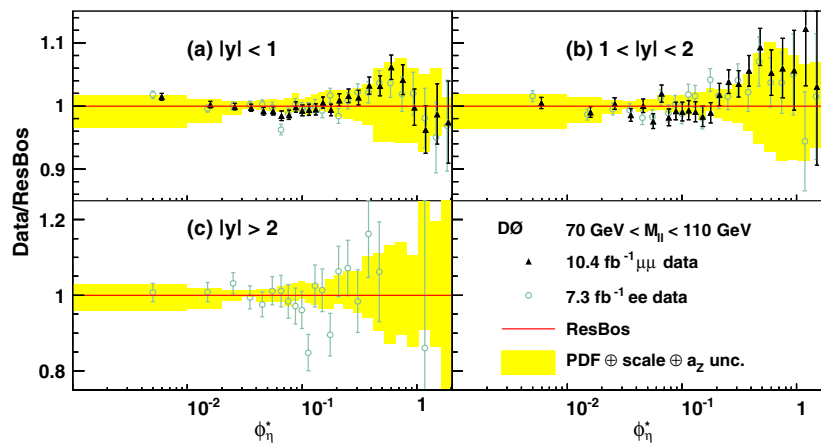


FIG. 3 (color online). Ratio of the corrected distributions of $(1/\sigma) \times (d\sigma/d\phi_\eta^*)$ in dielectron and dimuon data to the predictions of RESBOS [10] for $70 < M_{\ell\ell} < 110$ GeV for (a) $|y| < 1$, (b) $1 < |y| < 2$, and (c) $|y| > 2$. The error bars on the data points represent statistical and systematic uncertainties combined in quadrature. The dielectron data are taken from Ref. [1] and correspond to an integrated luminosity of 7.3 fb^{-1} . The band around the RESBOS prediction represents the quadrature sum of uncertainties due to PDFs, QCD scales, and the nonperturbative parameter a_Z .

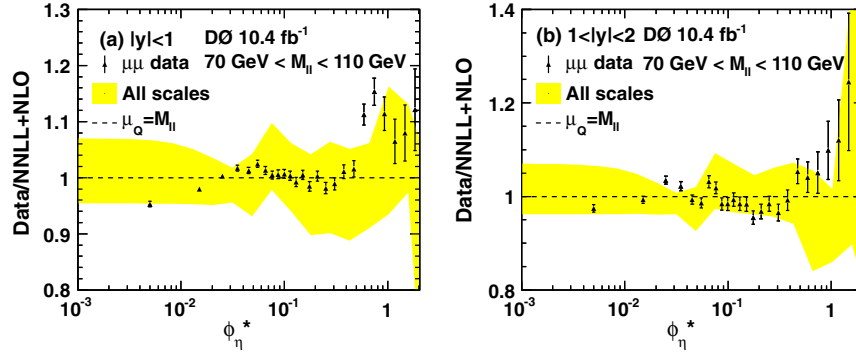


FIG. 4 (color online). Ratio of the corrected distributions of $(1/\sigma) \times (d\sigma/d\phi_\eta^*)$ in dimuon data to the NNLL + NLO predictions of Ref. [8] for $70 < M_{\ell\ell} < 110$ GeV: (a) $|y| < 1$ and (b) $1 < |y| < 2$. The error bars on the data points represent statistical and systematic uncertainties combined in quadrature. The band around the NNLL + NLO prediction represents the uncertainty due to variations in the QCD scales (evaluated by varying the resummation, factorization, and renormalization scales).

measurements represents a powerful cross-check of the corrected distributions.

Figure 4 shows for $70 < M_{\ell\ell} < 110$ GeV the ratio of the corrected dimuon data to the NNLL + NLO predictions of Ref. [8].

Figures 3–4 show that the theoretical uncertainties arising from QCD scale variations and PDFs are large compared to the experimental uncertainties. Within the quoted uncertainties both predictions are consistent with the corrected data. Figure 5 shows the ratio of the $(1/\sigma)(d\sigma/d\phi_\eta^*)$ distribution in the central rapidity region ($|y| < 1$) to that in the forward rapidity region ($1 < |y| < 2$). The corrected dimuon data are compared to the predictions from RESBOS [10] and from the NNLL + NLO calculations [8]. Figure 5 shows that the theoretical uncertainties largely cancel in this ratio and that the predictions are consistent with the data.

Figure 6 shows the normalized dimuon ϕ_η^* distributions $(1/\sigma) \times (d\sigma/d\phi_\eta^*)$ in two bins of $|y|$, corrected to the particle level with kinematic requirements: $30 < M_{\ell\ell} < 60$ GeV, and for both muons $|\eta| < 2$. The leading muon is required to satisfy $p_T > 15$ GeV and the second muon is required to satisfy $p_T > 10$ GeV. In addition, events are

required at particle level to contain no FSR photon with transverse energy $E_T^\gamma > 14$ GeV. The corrected data are compared to predictions from RESBOS [10] with the same particle-level kinematic cuts applied.

Figure 7 shows the ratio of the corrected ϕ_η^* distributions to the RESBOS predictions for $30 < M_{\ell\ell} < 60$ GeV. Figure 8 shows the ratio of the same data to the NNLL + NLO predictions of Ref. [8,27]. At high values of ϕ_η^* the prediction from RESBOS agrees less well with data than is the case in the region of the Z boson mass peak. A known deficiency of the RESBOS prediction for $\phi_\eta^* > 0.5$ in the low mass region is the absence of the NNLO correction factor for the photon exchange diagram.

Figure 9 shows the normalized dimuon ϕ_η^* distributions $(1/\sigma) \times (d\sigma/d\phi_\eta^*)$, corrected to the particle level with kinematic requirements: $160 < M_{\ell\ell} < 300$ GeV and $300 < M_{\ell\ell} < 500$ GeV, and for both muons $p_T > 15$ GeV and $|\eta| < 2$. The data are compared to predictions from RESBOS with the same particle-level kinematic requirements applied. Figure 10 shows the ratios of the corrected ϕ_η^* distributions to the RESBOS predictions. Within the fairly large statistical uncertainties, the predictions are consistent

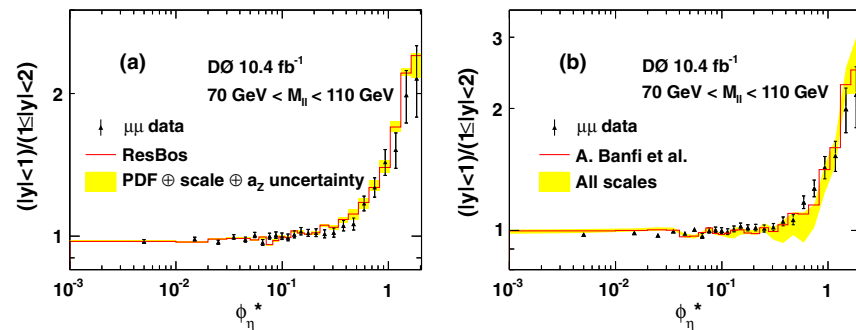


FIG. 5 (color online). Ratio of the $(1/\sigma)(d\sigma/d\phi_\eta^*)$ distribution in the central rapidity region ($|y| < 1$) to that in the forward rapidity region ($1 < |y| < 2$). The corrected dimuon data are compared to the predictions from (a) RESBOS [10] and from (b) NNLL + NLO [8]. The error bars on the data points represent statistical and systematic uncertainties combined in quadrature, assuming no correlation between the two rapidity regions. The theoretical predictions are represented by histograms and the band shows the theoretical uncertainties, taking correlations between the two rapidity regions into account.

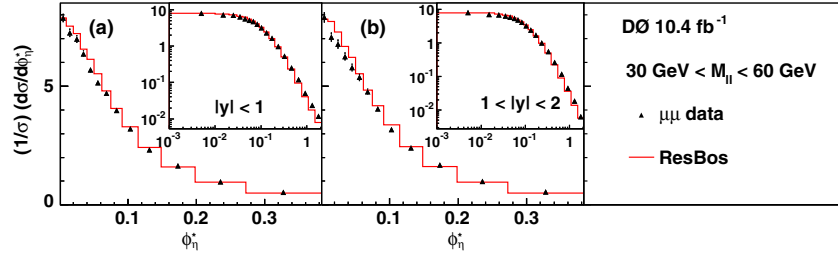


FIG. 6 (color online). Corrected distributions of $(1/\sigma) \times (d\sigma/d\phi_\eta^*)$ in dimuon events with $30 < M_{\ell\ell} < 60$ GeV for (a) $|y| < 1$ and (b) $1 < |y| < 2$ in the restricted range $0 < \phi_\eta^* < 0.38$. The insets show an extended range of ϕ_η^* . The error bars on the data points represent statistical and systematic uncertainties combined in quadrature. The predictions from RESBOS [10] are shown as histograms.

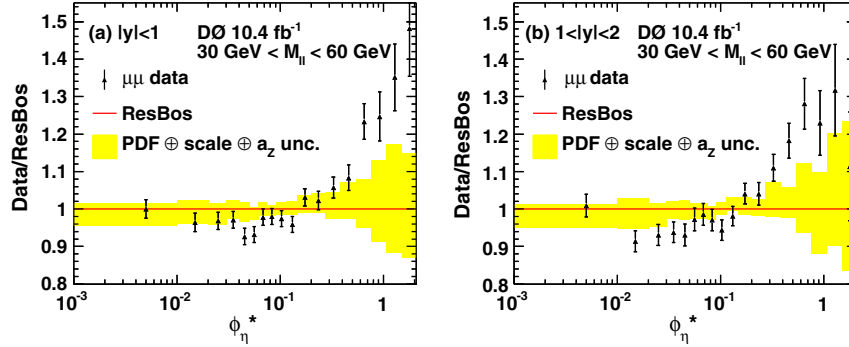


FIG. 7 (color online). Ratio of the corrected distributions of $(1/\sigma) \times (d\sigma/d\phi_\eta^*)$ to RESBOS [10] in dimuon events with $30 < M_{\ell\ell} < 60$ GeV for (a) $|y| < 1$ and (b) $1 < |y| < 2$. Statistical and systematic uncertainties are combined in quadrature. The band around the RESBOS prediction represents the quadrature sum of uncertainties due to PDFs, QCD scales, and the nonperturbative parameter a_z .

with the corrected data. As pointed out above there is no NNLO correction factor for the photon exchange diagram in RESBOS.

The corrected distributions of $(1/\sigma) \times (d\sigma/d\phi_\eta^*)$ in the two dimuon mass ranges $30 < M_{\ell\ell} < 60$ GeV and $70 < M_{\ell\ell} < 130$ GeV are compared in Fig. 11. As discussed above, the width of the ϕ_η^* distribution is expected to decrease with increasing $M_{\ell\ell}$. Figure 11 shows that the data are consistent with this expectation and that RESBOS provides a good description of this behavior. The numbers

of selected events in the dimuon mass ranges $160 < M_{\ell\ell} < 300$ GeV and $300 < M_{\ell\ell} < 500$ GeV are insufficient to allow us to present the distributions of $(1/\sigma) \times (d\sigma/d\phi_\eta^*)$ in the two separate ranges of $|y|$ shown in Fig. 11. However, the dependence on $|y|$ is small and a comparison between Figs. 9 and 11 shows that the distributions of $(1/\sigma) \times (d\sigma/d\phi_\eta^*)$ continue to become more narrow with increasing dimuon mass in the region above the Z boson mass peak.

In summary, using 10.4 fb^{-1} of $p\bar{p}$ collisions we have measured the normalized ϕ_η^* distribution $(1/\sigma) \times (d\sigma/d\phi_\eta^*)$

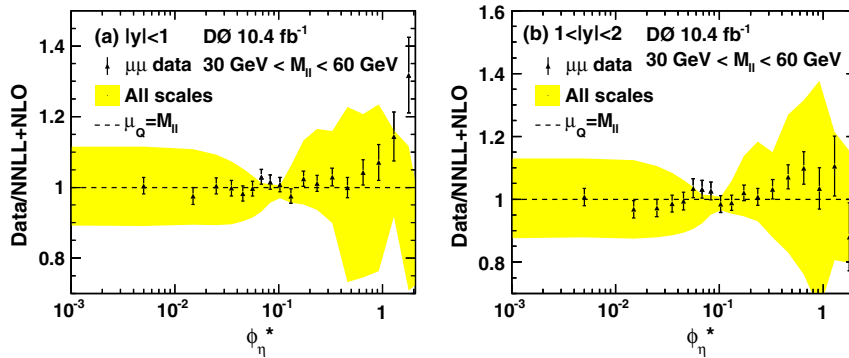


FIG. 8 (color online). Ratio of the corrected distributions of $(1/\sigma) \times (d\sigma/d\phi_\eta^*)$ to the NNLL + NLO predictions of Ref. [8,27] in dimuon events with $30 < M_{\ell\ell} < 60$ GeV for (a) $|y| < 1$ and (b) $1 < |y| < 2$. Statistical and systematic uncertainties are combined in quadrature. The band around the NNLL + NLO prediction represents the uncertainty due to variations in the QCD scales (evaluated by varying the resummation, factorization, and renormalization scales).

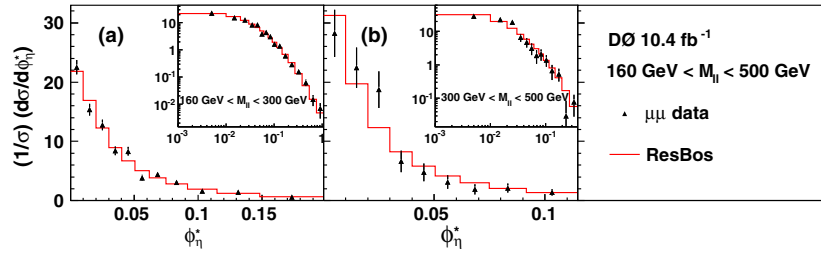


FIG. 9 (color online). Corrected distributions of $(1/\sigma) \times (d\sigma/d\phi_\eta^*)$ for dimuon events with (a) $160 < M_{\ell\ell} < 300$ GeV and (b) $300 < M_{\ell\ell} < 500$ GeV for a restricted range of ϕ_η^* . The insets show an extended range of ϕ_η^* . The error bars on the data points represent statistical and systematic uncertainties combined in quadrature. The predictions from RESBOS [10] are shown as the red histogram.

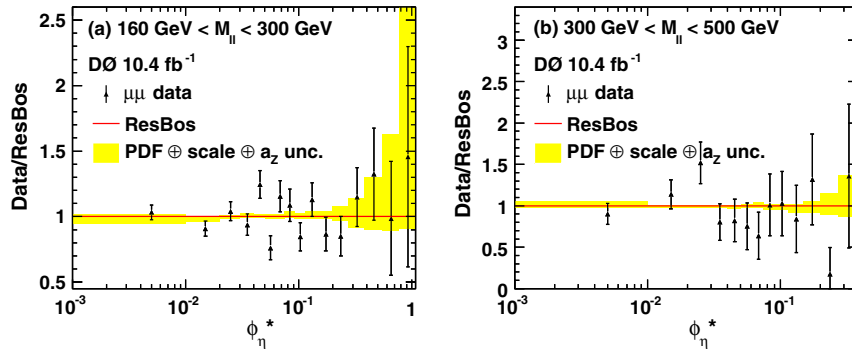


FIG. 10 (color online). Ratio of the corrected distributions of $(1/\sigma) \times (d\sigma/d\phi_\eta^*)$ to RESBOS [10] for (a) $160 < M_{\ell\ell} < 300$ GeV and (b) $300 < M_{\ell\ell} < 500$ GeV. Statistical and systematic uncertainties are combined in quadrature. The band around the RESBOS prediction represents the quadrature sum of uncertainties due to PDFs, QCD scales, and the nonperturbative parameter a_z .

in two bins of dimuon rapidity and four bins of dimuon mass. Relative to the results presented in Ref. [1], these measurements in the dimuon channel represent an extension to the full D0 data set and also to regions of dimuon mass away from the Z boson mass peak. The data are well described within the theoretical uncertainties by the RESBOS MC and by the predictions at NNLL + NLO accuracy of Ref. [8,27]. In the Z boson mass peak region, $70 < M_{\ell\ell} < 110$ GeV, the theoretical uncertainties shown in Figs. 3–4 are large compared to the experimental uncertainties. Figure 5 shows the ratio of the $(1/\sigma)(d\sigma/d\phi_\eta^*)$ distribution in the central rapidity region ($|y| < 1$) to that in the forward rapidity region ($1 < |y| < 2$). The theoretical

uncertainties largely cancel in this ratio and the QCD predictions are consistent with the data. The data are consistent with the expectation that the width of the ϕ_η^* distribution decreases with increasing $M_{\ell\ell}$. The measurements of ϕ_η^* distributions above the Z boson mass peak may help constrain systematic uncertainties arising from initial-state gluon bremsstrahlung in analyses of other high mass final states, such as those containing top quarks.

Tables I–VI of corrected $(1/\sigma) \times (d\sigma/d\phi_\eta^*)$ distributions for each $|y|$ bin and range of $M_{\ell\ell}$ are provided in the appendix. In some of these tables results are given for a larger range of ϕ_η^* than is shown in the corresponding figures.

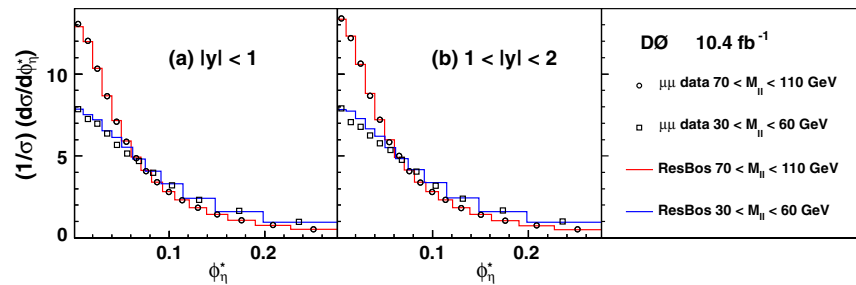


FIG. 11 (color online). Comparison of corrected distributions of $(1/\sigma) \times (d\sigma/d\phi_\eta^*)$ in dimuon events with $30 < M_{\ell\ell} < 60$ GeV and $70 < M_{\ell\ell} < 130$ GeV for (a) $|y| < 1$ and (b) $1 < |y| < 2$ in the restricted range $0 < \phi_\eta^* < 0.28$. The error bars on the data points represent statistical and systematic uncertainties combined in quadrature. The predictions from RESBOS [10] are shown as histograms.

ACKNOWLEDGMENTS

We thank the authors of Refs. [10] and [8], in particular Marco Guzzi and Lee Tomlinson, respectively, for their help in evaluating predictions to be compared with the new off-peak measurements. We thank the staff at Fermilab and collaborating institutions, and acknowledge support from the Department of Energy and National Science Foundation (United States of America); Alternative Energies and Atomic Energy Commission and National Center for Scientific Research/National Institute of Nuclear and Particle Physics (France); Ministry of Education and Science of the Russian Federation, National Research Center “Kurchatov Institute” of the Russian Federation, and Russian Foundation for Basic Research (Russia); National Council for the Development of Science and Technology and Carlos Chagas Filho Foundation for the Support of Research in the State of Rio de Janeiro (Brazil);

Department of Atomic Energy and Department of Science and Technology (India); Administrative Department of Science, Technology and Innovation (Colombia); National Council of Science and Technology (Mexico); National Research Foundation of Korea (Korea); Foundation for Fundamental Research on Matter (The Netherlands); Science and Technology Facilities Council and The Royal Society (United Kingdom); Ministry of Education, Youth and Sports (Czech Republic); Bundesministerium für Bildung und Forschung (Federal Ministry of Education and Research) and Deutsche Forschungsgemeinschaft (German Research Foundation) (Germany); Science Foundation Ireland (Ireland); Swedish Research Council (Sweden); China Academy of Sciences and National Natural Science Foundation of China (China); and Ministry of Education and Science of Ukraine (Ukraine).

APPENDIX: TABLES OF RESULTS

TABLE I. Table of results for the dimuon channel for $|y| < 1$ region with $70 < M_{\ell\ell} < 110$ GeV. The first quoted uncertainty is statistical and the second is the total experimental systematic uncertainty.

Bin	ϕ_η^* range	$1/\sigma \, d\sigma/d\phi_\eta^*$
1	0.000–0.010	$13.069 \pm 0.052 \pm 0.039$
2	0.010–0.020	$12.017 \pm 0.049 \pm 0.027$
3	0.020–0.030	$10.334 \pm 0.046 \pm 0.012$
4	0.030–0.040	$8.652 \pm 0.042 \pm 0.016$
5	0.040–0.050	$7.100 \pm 0.038 \pm 0.008$
6	0.050–0.060	$5.869 \pm 0.034 \pm 0.013$
7	0.060–0.071	$4.863 \pm 0.031 \pm 0.016$
8	0.071–0.081	$4.068 \pm 0.028 \pm 0.007$
9	0.081–0.093	$3.399 \pm 0.024 \pm 0.009$
10	0.093–0.106	$2.803 \pm 0.021 \pm 0.006$
11	0.106–0.121	$2.303 \pm 0.018 \pm 0.006$
12	0.121–0.139	$1.843 \pm 0.014 \pm 0.005$
13	0.139–0.162	$1.442 \pm 0.011 \pm 0.004$
14	0.162–0.190	$1.067 \pm 0.009 \pm 0.003$
15	0.190–0.227	$0.778 \pm 0.007 \pm 0.002$
16	0.227–0.275	$0.524 \pm 0.005 \pm 0.002$
17	0.275–0.337	$0.332 \pm 0.003 \pm 0.002$
18	0.337–0.418	$0.204 \pm 0.002 \pm 0.001$
19	0.418–0.523	$0.115 \pm 0.002 \pm 0.001$
Bin	Range	$1/\sigma \times (d\sigma/d\phi_\eta^*)(\times 100)$
20	0.523–0.657	$6.428 \pm 0.099 \pm 0.040$
21	0.657–0.827	$3.310 \pm 0.064 \pm 0.029$
22	0.827–1.041	$1.673 \pm 0.041 \pm 0.019$
23	1.041–1.309	$0.818 \pm 0.026 \pm 0.016$
24	1.309–1.640	$0.420 \pm 0.017 \pm 0.010$
25	1.640–2.049	$0.225 \pm 0.011 \pm 0.010$
26	2.049–2.547	$0.120 \pm 0.007 \pm 0.005$
27	2.547–3.151	$0.076 \pm 0.005 \pm 0.004$
28	3.151–3.878	$0.044 \pm 0.004 \pm 0.003$
29	3.878–4.749	$0.026 \pm 0.003 \pm 0.001$

TABLE II. Table of results for the dimuon channel for $1 < |y| < 2$ region with $70 < M_{\ell\ell} < 110$ GeV. The first quoted uncertainty is statistical and the second is the total experimental systematic uncertainty.

Bin	ϕ_η^* range	$1/\sigma \, d\sigma/d\phi_\eta^*$
1	0.000–0.010	$13.404 \pm 0.094 \pm 0.056$
2	0.010–0.020	$12.189 \pm 0.090 \pm 0.036$
3	0.020–0.030	$10.635 \pm 0.084 \pm 0.027$
4	0.030–0.040	$8.685 \pm 0.076 \pm 0.030$
5	0.040–0.050	$7.218 \pm 0.069 \pm 0.022$
6	0.050–0.060	$5.836 \pm 0.062 \pm 0.017$
7	0.060–0.071	$5.013 \pm 0.057 \pm 0.027$
8	0.071–0.081	$4.065 \pm 0.050 \pm 0.011$
9	0.081–0.093	$3.382 \pm 0.044 \pm 0.009$
10	0.093–0.106	$2.802 \pm 0.038 \pm 0.010$
11	0.106–0.121	$2.317 \pm 0.032 \pm 0.007$
12	0.121–0.139	$1.827 \pm 0.026 \pm 0.007$
13	0.139–0.162	$1.407 \pm 0.020 \pm 0.008$
14	0.162–0.190	$1.050 \pm 0.016 \pm 0.003$
15	0.190–0.227	$0.764 \pm 0.012 \pm 0.005$
16	0.227–0.275	$0.518 \pm 0.008 \pm 0.002$
17	0.275–0.337	$0.326 \pm 0.006 \pm 0.002$
18	0.337–0.418	$0.194 \pm 0.004 \pm 0.001$
19	0.418–0.523	$0.109 \pm 0.003 \pm 0.001$
Bin	Range	$1/\sigma \times (d\sigma/d\phi_\eta^*)(\times 100)$
20	0.523–0.657	$5.478 \pm 0.166 \pm 0.050$
21	0.657–0.827	$2.610 \pm 0.102 \pm 0.040$
22	0.827–1.041	$1.167 \pm 0.061 \pm 0.026$
23	1.041–1.309	$0.538 \pm 0.038 \pm 0.017$
24	1.309–1.640	$0.212 \pm 0.022 \pm 0.011$
25	1.640–2.049	$0.104 \pm 0.015 \pm 0.008$
26	2.049–2.547	$0.046 \pm 0.009 \pm 0.005$
27	2.547–3.151	$0.022 \pm 0.006 \pm 0.003$
28	3.151–3.878	$0.013 \pm 0.004 \pm 0.002$
29	3.878–4.749	$0.009 \pm 0.003 \pm 0.001$

TABLE III. Table of results for the dimuon channel for $|y| < 1$ region $30 < M_{\ell\ell} < 60$ GeV. The first quoted uncertainty is statistical and the second is the total experimental systematic uncertainty.

Bin	ϕ_η^* range	$1/\sigma \, d\sigma/d\phi_\eta^*$
1	0.000–0.010	$7.87 \pm 0.14 \pm 0.12$
2	0.010–0.020	$7.25 \pm 0.13 \pm 0.12$
3	0.020–0.030	$6.98 \pm 0.13 \pm 0.09$
4	0.030–0.040	$6.36 \pm 0.12 \pm 0.06$
5	0.040–0.051	$5.68 \pm 0.11 \pm 0.05$
6	0.051–0.062	$5.15 \pm 0.10 \pm 0.03$
7	0.062–0.075	$4.70 \pm 0.09 \pm 0.03$
8	0.075–0.092	$3.98 \pm 0.08 \pm 0.02$
9	0.092–0.115	$3.21 \pm 0.06 \pm 0.03$
10	0.115–0.148	$2.32 \pm 0.04 \pm 0.03$
11	0.148–0.198	$1.65 \pm 0.03 \pm 0.02$
12	0.198–0.273	$0.98 \pm 0.02 \pm 0.01$
Bin	Range	$1/\sigma \times (d\sigma/d\phi_\eta^*)(\times 100)$
13	0.273–0.382	$52.61 \pm 1.07 \pm 0.73$
14	0.382–0.541	$25.07 \pm 0.63 \pm 0.35$
15	0.541–0.766	$11.88 \pm 0.36 \pm 0.18$
16	0.766–1.080	$5.05 \pm 0.21 \pm 0.11$
17	1.080–1.509	$2.36 \pm 0.12 \pm 0.07$
18	1.509–2.087	$1.17 \pm 0.08 \pm 0.06$
19	2.087–2.853	$0.40 \pm 0.04 \pm 0.03$
20	2.853–3.853	$0.19 \pm 0.02 \pm 0.02$

TABLE IV. Table of results for the dimuon channel for $1 < |y| < 2$ region $30 < M_{\ell\ell} < 60$ GeV. The first quoted uncertainty is statistical and the second is the total experimental systematic uncertainty.

Bin	ϕ_η^* range	$1/\sigma \, d\sigma/d\phi_\eta^*$
1	0.000–0.010	$7.89 \pm 0.19 \pm 0.12$
2	0.010–0.020	$7.06 \pm 0.18 \pm 0.10$
3	0.020–0.030	$6.77 \pm 0.17 \pm 0.09$
4	0.030–0.040	$6.25 \pm 0.16 \pm 0.05$
5	0.040–0.051	$5.78 \pm 0.16 \pm 0.06$
6	0.051–0.062	$5.37 \pm 0.14 \pm 0.06$
7	0.062–0.075	$4.76 \pm 0.13 \pm 0.02$
8	0.075–0.092	$4.05 \pm 0.10 \pm 0.04$
9	0.092–0.115	$3.18 \pm 0.08 \pm 0.04$
10	0.115–0.148	$2.40 \pm 0.06 \pm 0.02$
11	0.148–0.198	$1.68 \pm 0.04 \pm 0.02$
12	0.198–0.273	$1.00 \pm 0.02 \pm 0.01$
Bin	Range	$1/\sigma \times (d\sigma/d\phi_\eta^*)(\times 100)$
13	0.273–0.382	$54.80 \pm 1.48 \pm 0.70$
14	0.382–0.541	$26.13 \pm 0.85 \pm 0.38$
15	0.541–0.766	$11.51 \pm 0.49 \pm 0.25$
16	0.766–1.080	$4.39 \pm 0.26 \pm 0.10$
17	1.080–1.509	$1.82 \pm 0.15 \pm 0.06$
18	1.509–2.087	$0.63 \pm 0.07 \pm 0.02$
19	2.087–2.853	$0.26 \pm 0.04 \pm 0.03$
20	2.853–3.853	$0.17 \pm 0.04 \pm 0.02$

TABLE V. Table of results for the dimuon channel for $160 < M_{\ell\ell} < 300$ GeV region. The first quoted uncertainty is statistical and the second is the total experimental systematic uncertainty.

Bin	ϕ_η^* range	$1/\sigma \, d\sigma/d\phi_\eta^*$
1	0.000–0.010	$22.48 \pm 1.18 \pm 0.35$
2	0.010–0.020	$15.34 \pm 0.97 \pm 0.18$
3	0.020–0.030	$12.73 \pm 0.88 \pm 0.15$
4	0.030–0.040	$8.40 \pm 0.72 \pm 0.13$
5	0.040–0.051	$8.32 \pm 0.70 \pm 0.11$
6	0.051–0.062	$3.87 \pm 0.46 \pm 0.09$
7	0.062–0.075	$4.41 \pm 0.45 \pm 0.10$
8	0.075–0.092	$3.06 \pm 0.33 \pm 0.10$
9	0.092–0.115	$1.65 \pm 0.21 \pm 0.03$
10	0.115–0.148	$1.40 \pm 0.16 \pm 0.02$
11	0.148–0.198	$0.60 \pm 0.09 \pm 0.02$
Bin	Range	$(1/\sigma) \times (d\sigma/d\phi_\eta^*) \times 100$
12	0.198–0.273	$28.48 \pm 4.98 \pm 0.74$
13	0.273–0.382	$15.55 \pm 2.98 \pm 0.60$
14	0.382–0.541	$6.27 \pm 1.64 \pm 0.33$
15	0.541–0.766	$1.50 \pm 0.65 \pm 0.12$
16	0.766–1.080	$0.69 \pm 0.39 \pm 0.07$

TABLE VI. Table of results for the dimuon channel for $300 < M_{\ell\ell} < 500$ GeV region. The first quoted uncertainty is statistical and the second is the total experimental systematic uncertainty.

Bin	ϕ_η^* range	$1/\sigma \, d\sigma/d\phi_\eta^*$
1	0.000–0.010	$28.17 \pm 3.93 \pm 0.57$
2	0.010–0.020	$22.38 \pm 3.40 \pm 0.34$
3	0.020–0.030	$18.70 \pm 3.06 \pm 0.41$
4	0.030–0.040	$6.61 \pm 1.80 \pm 0.18$
5	0.040–0.051	$4.76 \pm 1.48 \pm 0.10$
6	0.051–0.062	$3.14 \pm 1.16 \pm 0.12$
7	0.062–0.075	$1.91 \pm 0.84 \pm 0.14$
8	0.075–0.092	$2.11 \pm 0.78 \pm 0.06$
9	0.092–0.115	$1.40 \pm 0.53 \pm 0.06$
10	0.115–0.148	$0.68 \pm 0.30 \pm 0.12$
11	0.148–0.198	$0.54 \pm 0.22 \pm 0.04$
Bin	Range	$(1/\sigma) \times (d\sigma/d\phi_\eta^*) \times 100$
12	0.198–0.273	$2.98 \pm 5.47 \pm 0.21$
13	0.273–0.382	$7.78 \pm 4.95 \pm 0.47$
14	0.382–0.412	$2.24 \pm 2.57 \pm 0.20$

- [1] V.M. Abazov *et al.* (D0 Collaboration), *Phys. Rev. Lett.* **106**, 122001 (2011).
- [2] A. Banfi, S. Redford, M. Vesterinen, P. Waller, and T.R. Wyatt, *Eur. Phys. J. C* **71**, 1600 (2011).
- [3] The dilepton rapidity is defined by $y = (1/2) \ln[(E + p_z)/(E - p_z)]$, where E is the energy and p_z is the momentum component parallel to the proton beam direction. The rapidity is given in terms of the momentum fractions, x_1 and x_2 , of the annihilating quark and antiquark by $y = (1/2) \ln(x_1/x_2)$.
- [4] Pseudorapidity is defined by $\eta = -\ln[\tan(\theta/2)]$, where θ is the polar angle with respect to the proton beam direction.
- [5] M. Vesterinen and T.R. Wyatt, *Nucl. Instrum. Methods Phys. Res., Sect. A* **602**, 432 (2009).
- [6] The thrust axis is defined as a unit vector in the direction of $\vec{p}_T^{(\text{lepton } 1)} - \vec{p}_T^{(\text{lepton } 2)}$, where $\vec{p}_T^{(\text{lepton } 1)}$ and $\vec{p}_T^{(\text{lepton } 2)}$ are the lepton momentum vectors in the transverse plane.
- [7] A. Banfi, M. Dasgupta, and S. Marzani, *Phys. Lett. B* **701**, 75 (2011).
- [8] A. Banfi, M. Dasgupta, S. Marzani, and L. Tomlinson, *J. High Energy Phys.* **01** (2012) 044.
- [9] J. M. Campbell and R. K. Ellis, *Phys. Rev. D* **65**, 113007 (2002).
- [10] M. Guzzi, P. M. Nadolsky, and B. Wang, *Phys. Rev. D* **90**, 014030 (2014).
- [11] A. Banfi, M. Dasgupta, S. Marzani, and L. Tomlinson, *Phys. Lett. B* **715**, 152 (2012).
- [12] G. Aad *et al.* (ATLAS Collaboration), *Phys. Lett. B* **720**, 32 (2013).
- [13] R. Aaij *et al.* (LHCb Collaboration), *J. High Energy Phys.* **02** (2013) 106.
- [14] J. Collins, D. Soper, and G. Sterman, *Nucl. Phys.* **B250**, 199 (1985).
- [15] V.M. Abazov *et al.* (D0 Collaboration), *Nucl. Instrum. Methods Phys. Res., Sect. A* **565**, 463 (2006); M. Abolins *et al.*, *Nucl. Instrum. Methods Phys. Res., Sect. A* **584**, 75 (2008); R. Angstadt *et al.*, *Nucl. Instrum. Methods Phys. Res., Sect. A* **622**, 298 (2010).
- [16] S. Abachi *et al.* (D0 Collaboration), *Nucl. Instrum. Methods Phys. Res., Sect. A* **338**, 185 (1994).
- [17] V.M. Abazov *et al.*, *Nucl. Instrum. Methods Phys. Res., Sect. A* **552**, 372 (2005).
- [18] T. Sjöstrand, P. Edén, C. Friberg, L. Lönnblad, G. Miu, S. Mrenna, and E. Norrbin, *Comput. Phys. Commun.* **135**, 238 (2001).
- [19] R. Brun and F. Carminati, CERN Report No. W5013, 1993 (unpublished).
- [20] M. L. Mangano, F. Piccinini, A. D Polosa, M. Moretti, and R. Pittau, *J. High Energy Phys.* **07** (2003) 001.
- [21] C. Balazs and C.-P. Yuan, *Phys. Rev. D* **56**, 5558 (1997).
- [22] Following Ref. [10] the central value of the nonperturbative parameter $a_Z = 1.1 \text{ GeV}^2$ is chosen in RESBOS. The central values of the QCD scale parameters of the CSS formalism [14] used in RESBOS are chosen to be $C_1 = C_3 = 2b_0$ and $C_2 = C_4 = 1/2$, where $b_0 = e^{-\gamma_E} \approx 1.123$, where $\gamma_E \approx 0.577$ is the Euler-Mascheroni constant. In assigning uncertainties to the predictions of RESBOS the value of a_Z is varied over the range $1.05 < a_Z < 1.19 \text{ GeV}^2$. The QCD scale uncertainties for the RESBOS predictions are evaluated by varying independently the scale parameters C_1 , C_2 , and C_3 up and down by a factor of two relative to the central values given above. The relationship $C_2 = C_4$ is maintained throughout. The overall QCD scale uncertainty is taken as the quadrature sum of the changes in the predicted $(1/\sigma) \times (d\sigma/d\phi_\eta^*)$ resulting from the variations in C_1 , C_2 , and C_3 .
- [23] J. Gao, M. Guzzi, J. Huston, H.-L. Lai, Z. Li, P.M. Nadolsky, J. Pumplin, D. Stump, and C.-P. Yuan, *Phys. Rev. D* **89**, 033009 (2014).
- [24] E. Barberio and Z. Was, *Comput. Phys. Commun.* **79**, 291 (1994).
- [25] J. Pumplin, D. R. Stump, J. Huston, H. L. Lai, P. Nadolsky, and W. K. Tung, *J. High Energy Phys.* **07** (2002) 012.
- [26] Following Ref. [1] the momentum of MC particle-level electrons is defined as the full-momentum vector sum of any photons or electrons within a cone of $\Delta R = \sqrt{(\Delta\eta)^2 + (\Delta\phi)^2} < 0.2$ around the electron, where $\Delta\eta$ ($\Delta\phi$) is the distance in η (ϕ) from the particle-level electron. The dielectron kinematic requirements are $70 < M_{\ell\ell} < 110 \text{ GeV}$, and for both electrons $p_T > 20 \text{ GeV}$ and $|\eta| < 1.1$ or $1.5 < |\eta| < 3$.
- [27] L. Tomlinson (private communication).